RSC Advances

PAPER

View Article Online
View Journal | View Issue

Cite this: *RSC Adv.*, 2026, **16**, 1848

Synthesis, crystal structure and DFT studies of a methylphenyl piperazinyl dithiocarbamato zinc(II) precursor for zinc sulfide nanophotocatalysts used for the degradation of trypan blue and rhodamine 6G dyes

Peter A. Ajibade, *[a] Fartisincha P. Andrew,[a] Thandi B. Mbuyazi,[a] Tshephiso R. Papo[a] and Krishnan Rajeshwar[b]

A 1-(4-methylphenyl)piperazinyl dithiocarbamato-*S*,*S*′ Zn(II) complex was prepared, and its molecular structure was determined using single-crystal X-ray crystallography. The zinc(II) dithiocarbamate compound crystallized as a dimeric structure with two zinc(II) ions that are coordinated to two molecules of 1-(4-methylphenyl)piperazinyl dithiocarbamato anions as bidentate chelating ligands. In addition, the sulfur atom of the adjacent centrosymmetric molecule is coordinated to the adjacent Zn(II) ion. The geometry and electronic properties optimized using DFT and the HOMO–LUMO energies matched the experimental findings. The complex was thermolyzed in octadecylamine (ODA), dodecylamine (DDA), and hexadecylamine (HDA) to prepare zinc sulfide nanoparticles: ZnS-ODA, ZnS-DDA, and ZnS-HDA. The as-prepared zinc sulfide nanoparticles were used as photocatalysts for the degradation of trypan blue and rhodamine 6G dyes. The photocatalytic degradation of trypan blue by ZnS-ODA showed the highest photocatalytic efficiency of 95.71%, while ZnS-DDA degraded 83.21% of rhodamine 6G after 180 min. The degradation process followed pseudo-first-order kinetics with rate constants of 1.69×10^{-2} min^{-1}, 5.18×10^{-3} min^{-1}, and 6.75×10^{-3} min^{-1} for trypan blue dye and 3.54×10^{-3} min^{-1}, 7.44×10^{-3} min^{-1}, and 6.21×10^{-3} min^{-1} for rhodamine 6G dye by ZnS-ODA, ZnS-DDA, and ZnS-HDA, respectively. The results indicate the potential of the as-prepared ZnS nanoparticles as effective photocatalysts for trypan blue and rhodamine 6G dyes degradation.

Received 3rd July 2025
Accepted 20th December 2025

DOI: 10.1039/d5ra04748j

rsc.li/rsc-advances

1. Introduction

Metal dithiocarbamate complexes are versatile coordination compounds that are of significant research interest due to their diverse structural motif and different applications.[1–5] There has been growing interest in the use of metal dithiocarbamate complexes as single-source precursors for the preparation of metal sulfide nanoparticles.[6–9] Among these, zinc(II) dithiocarbamates have become preferred candidates for synthesizing zinc sulfide nanoparticles (ZnS-NPs)[10–12] because of their specific chemical composition and unique properties.[13–15] These complexes consist of both the zinc metal and sulfur within a single molecular framework. There are several methods for the preparation of zinc sulfide nanoparticles, but the thermal decomposition of zinc(II) dithiocarbamate complexes as single-source precursors has received considerable attention.[16–18] The method allows the precise control of reaction parameters, such as temperature, capping agent, and time, to prepare well-defined ZnS nanoparticles tuned for specific applications. The single-source precursor undergoes a clean decomposition to produce stoichiometric ZnS with minimal impurities and eliminates the need for an external sulfur source.

In recent years, semiconductor nanoparticles are being used as photocatalysts for the degradation of organic dyes.[19–21] Trypan blue and rhodamine 6G are synthetic diazo and cationic xanthene dyes that are widely used in industries.[22–24] Due to their high stability, color intensity, and potential toxicity, these dyes are considered harmful to the environment.[25,26] Methods such as adsorption, oxidation, and photodegradation have been used to remove dye contaminants from water,[27] but recent studies have shown that the use of semiconductor nanoparticles as photocatalysts is an effective technique for the degradation of organic dyes.[28–30] Zinc sulfide nanoparticles have demonstrated remarkable photodegradation efficiency for various organic dyes under UV or visible light irradiation.[31] In this study, we present the preparation and molecular structure of a 1-(4-methylphenyl)piperazinyl dithiocarbamate-*S*,*S*′ Zn(II)

[a]*School of Chemistry and Physics, University of KwaZulu-Natal, Private Bag X01, Scottsville, Pietermaritzburg, 3209, South Africa. E-mail: ajibadep@ukzn.ac.za*
[b]*Department of Chemistry & Biochemistry, The University of Texas at Arlington, Arlington, Texas 76109, USA*

complex. Theoretical studies were used to determine the molecular and electronic structure of the complex. The Zn(II) complex was used as a single-source precursor to prepare zinc sulfide nanophotocatalysts in three different capping agents: octadecylamine (ODA), dodecylamine (DDA), and hexadecylamine (HDA) for the degradation of trypan blue and rhodamine 6G dyes under visible light irradiation.

2. Experimental

2.1. Materials

1-(4-Methylphenyl)piperazine, sodium hydroxide, zinc(II) chloride, carbon disulfide, trioctylphosphine, octadecylamine, and dodecylamine were purchased from Sigma Aldrich, USA. Hexadecylamine was obtained from Merck Schuchardt OHG, Germany. All solvents were used as obtained without further purification.

2.2. Characterization techniques

The absorption spectra of the ZnS nanoparticles were measured with a PerkinElmer Lambda 25 UV-Vis spectrophotometer in the wavelength range of 200–700 nm. The samples were dispersed in methanol and sonicated to ensure uniform suspension prior to measurement. The spectra were measured using a quartz cuvette with a path length of 1 cm. Baseline correction was performed using methanol as a reference. FTIR spectra were recorded using a Bruker Alpha II instrument fitted with a platinum attenuated total reflectance (ATR) accessory. The nuclear magnetic resonance (NMR) spectra of the ligand and zinc(II) dithiocarbamate were recorded in deuterated water and DMSO using a Bruker 400 MHz spectrometer. Mass spectra were recorded using a Waters Micromass LCT Premier instrument having an electron spray ionization (ESI) source and time-of-flight (TOF) mass analyzer. Elemental analysis (CHNS) was recorded using a CHNS-O Flash 2000 elemental analyzer. Electron microscopy was performed using SEM-EDS and TEM images, which were obtained with a Zeiss EVO LS15 microscope and a JEOL JEM 1400 electron microscope, respectively.

2.3. Preparation of 1-(4-methylphenyl)piperazinyl dithiocarbamate and the zinc(II) complex

The ligand, 1-(4-methylphenyl)piperazinyl dithiocarbamate, and the complex were prepared using a previously reported method.[32] Sodium hydroxide (0.008 mole, 0.32 g) and 1-(4-methyl phenyl) piperazine (0.008 mole, 1.4101 g) were magnetically stirred at room temperature for 20 minutes. The temperature was then reduced to 4 °C, and carbon disulfide (0.008 mole, 0.5 mL) was added and stirred for 3 h. The white product was filtered, washed and dried. Yield: 91.45% color: white solid, UV-Vis (H_2O, λ_{max}, nm) 254, 294, ^{1}H NMR (400 MHz, D_2O, δ, ppm), 7.07–7.09 (d 2H), 6.90–6.92 (d, 2H), 4.58–4.60 (t, 4H), 3.14–3.17 (t, 4H), 2.26 (s, 3H). ^{13}C NMR (400 MHz, D_2O, δ, ppm), 212.23 (CS), 149.01, 129.43, 129.16, 116.61 (–C_6H_5), 50.13, 49.65 (–CH_4NCH_4–), 19.11 (–CH_3). Selected FTIR ν (cm^{-1}); 916–1001 (C–S), 1212 (C–N), 1417 (C═S),1514 (C–C), 1617 (C═C), 2908, 2813 (–CH_2), 3376, 3271, 3200 (C–H).

The zinc(II) dithiocarbamate was prepared from the reaction of an aqueous solution of the 1-(4-methylphenyl)piperazinyl dithiocarbamate ligand (0.002 mole, 0.5488 g) and zinc(II) chloride (0.001 mole, 0.1363 g). The mixture was stirred for 3 h at room temperature, and the white product was filtered, washed with distilled water and dried over silica. Crystals suitable for single-crystal X-ray crystallography were obtained from a DMSO solution of the compound layered with methanol. Yield: 80.30% color: white solid, UV-Vis (DCM, λ_{max}, nm) 253, 281. HSQC-NMR (400 MHz, DMSO, δ, ppm), 7.05 (d 2H), 6.87 (d, 2H), 4.16 (t, 4H), 3.18 (t, 4H), 2.21 (s, 3H). Selected FTIR ν (cm^{-1}); 927–1012, (C–S), 1229 (C–N), 1432 (C═S), 1507 (C–C), 1614 (C═C), 2815, 2823 (–CH_2), 2980 (C–H). $m/z = 565$ g mol^{-1}.

2.4. Single-crystal X-ray determination

Crystal structure determinations for the 1-(4-methylphenyl) piperazinyl dithiocarbamato-*S*,*S*′ zinc(II) complex were conducted on a Bruker APEX-II CCD diffractometer (Billerica, MA, USA) using graphite monochromated Mo-Ka($\lambda = 0.71073$ Å) radiation at 200 K. The structure of the compound was solved with SHELXT and refined using programs, such as Olex2 and SHELXT.[33–35]

2.5. Computational analysis

2.5.1. Hirshfeld surface analysis. A Hirshfeld surface analysis of the compound was carried out using CrystalExplorer 17.5. This analysis evaluates the intermolecular interactions induced by hydrogen bond donors and acceptors within a crystal structure, detailing the spatial occupation of a molecule within the crystal. It also visualizes the van der Waals (vdW) surface around the molecule.[36]

2.5.2. Computational modelling of the molecular and electronic properties of the zinc(II) compound. The molecular and electronic properties of the compound were optimized and determined in the gas phase *via* computational modelling, using the B3LYP method with a 6-31G basis set. Gaussian 09W software[37] was utilized for optimization, and the results were visualized using GaussView 5.0. The energy gap between the highest occupied molecular orbital (ΔE_{HOMO}) and the lowest unoccupied molecular orbital (ΔE_{LUMO}) was calculated using Koopmans' theorem.[38] Additionally, the potential nucleophilic and electrophilic reactive sites on the complex's molecular surface were identified by the molecular electrostatic potential (MEP) map at the surface of the electron cloud.

2.6. Synthesis of zinc sulfide nanoparticles

4 g of each capping agent (hexadecylamine (HDA), dodecylamine (DDA), and octadecylamine (ODA)) was added separately to a three-necked round-bottom flask equipped with a reflux condenser, rubber septum, and thermometer. The setup was purged with nitrogen gas and heated to 150 °C under continuous gas flow until each capping agent melted. A solution of the zinc(II) dithiocarbamate complex (0.4 g) in 2 mL of trioctylphosphine (TOP) was then rapidly injected into each molten capping agent. The reaction temperature was kept at 150 °C under an inert atmosphere for 1 h. The mixture was cooled to 70 °C, and the zinc sulfide nanoparticles were

precipitated with cold methanol. The precipitate was collected by centrifugation, washed several times with cold methanol, and dried under vacuum. The resulting nanoparticles were labeled as ZnS-ODA, ZnS-DDA, and ZnS-HDA, based on the respective capping agents.

2.7. Photocatalysis experiments

The photocatalytic activity of the nanoparticles was assessed for the degradation of 10 mg L^{-1} aqueous solutions of trypan blue and rhodamine 6G dyes. In the experiment, 0.05 g of each of the nanoparticles (photocatalyst) was mixed with a 5 mL aqueous solution of each dye (10 mg L^{-1}). The mixture was sonicated for 30 minutes and then stirred in the dark for 60 min to achieve the adsorption–desorption equilibrium of the dye on the surface of the catalyst. Subsequently, the dye–catalyst mixture was exposed to visible light for 180 minutes using an OSRAM HQL (MBF-U) 125 W lamp as the source. Samples of approximately 5 mL were collected at 30-minute intervals, and the absorbance was measured. The percentage dye degradation efficiency was evaluated using eqn (1).

$$\text{Efficiency}(\%) = \frac{C_0 - C_t}{C_0} \times 100 \quad (1)$$

where C_0 and C_t are the initial concentration and concentration of the dye at time (t), respectively.[39]

A pseudo-first order kinetic model was adopted given by eqn (2).

$$\ln\frac{C_0}{C_t} = kt \quad (2)$$

where k is the rate constant, and C_0 and C_t are the initial concentration and concentration of the dye at time (t), respectively.

The half-life ($t_{1/2}$) was also determined using eqn (3).

$$t_{1/2} = \frac{0.693}{k} \quad (3)$$

2.8. Determination of reactive species

A quenching experiment was used to determine the reactive species responsible for the photodegradation of trypan blue and rhodamine 6G dyes by the ZnS nanoparticles. Benzoquinone (BQ), isopropyl alcohol (IPA), and silver nitrate (SN) were used as $^{\bullet}O_2^-$, $^{\bullet}OH$, and e^- quenchers, respectively.[28] 10 mM of each scavenger was added to the dye–catalyst mixture, and the reaction was performed under the same parameters as the photocatalysis experiment.

3. Results and discussion

3.1. Spectroscopic studies of the dithiocarbamate ligand and zinc(II) complex

Proton, and carbon-13 NMR, as well as mass spectrometry data (Fig. S1–S5) confirmed the successful preparation of the compounds. The FTIR spectra of the ligand and complex (Fig. S6A) exhibit characteristic strong bands in the range 3374–2813 cm^{-1} corresponding to ν (C–H) and ν ($-CH_2$), respectively. These bands became weak and shifted in the complex to 2824–2917 cm^{-1}. Sharp bands at 1614 and 1617 cm^{-1} in the spectrum of the ligand are ascribed to the ν (C=C) of the *p*-tolyl moiety. Sharp bands observed at 1514 and 1417 cm^{-1} in the ligand were ascribed to C–C and C=S stretching vibrations, respectively. These bands were observed at 1507 and 1432 cm^{-1} in the zinc(II) complex, respectively. The C–N stretching vibration was observed at 1212 cm^{-1} in the ligand and shifted to 1229 cm^{-1} in the complex. The ν (C–S) observed at 916 cm^{-1} in the ligand shifted to a higher wave number upon coordination to the zinc(II) ions. The decrease in intensity is ascribed to the delocalization of the π-electrons within the dithiocarbamato moiety, which is typical of a bidentately coordinated dithiocarbamate ligand.[40] The electronic spectra of the ligand and zinc(II) complex (Fig. S6 B1 and B2) showed two absorptions at 254 and 294 nm, respectively, which are due to intra-ligand charge transfer transitions. These absorptions shifted to 253 and 281 nm, respectively, upon coordination in the complex owing to charge transfer transitions for the filled d-orbitals of the zinc(II) complex to the ligand orbitals.[41]

3.2. Molecular structure of the Zn(II) dithiocarbamate complex

The molecular structure of the Zn(II) dithiocarbamate complex is shown in Fig. 1 and crystal packing in Fig. 2. The crystal data

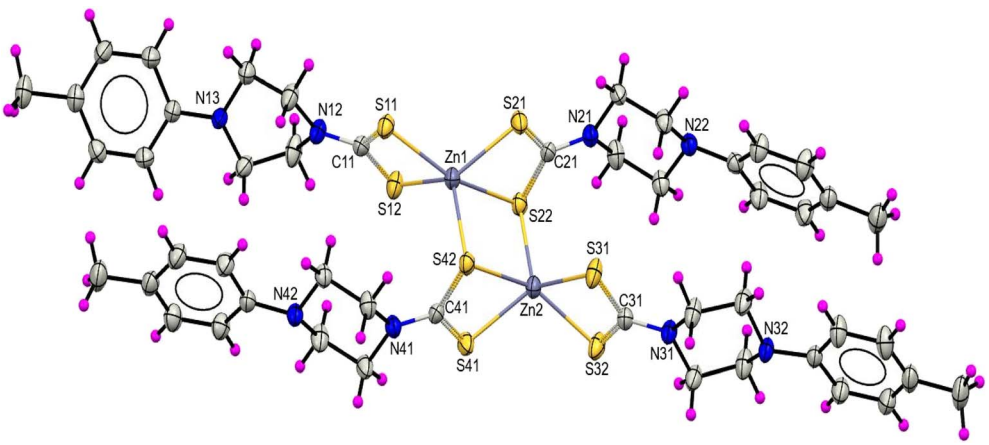

Fig. 1 Crystal structure of the 1-(4-methylphenyl)piperazinyl-dithiocarbamato Zn(II) complex.

Table 1 Single-crystal data and structure refinement of the Zn(II) complex

Formula	$C_{48}H_{60}N_8S_8Zn_2$
Formula weight	1136.30
Crystal system	Triclinic
Space group	*P*1
a(Å)	9.8071 (3)
b(Å)	15.3901 (5)
c(Å)	17.9139 (6)
α(°)	72.8133 (13)
β(°)	81.7075 (12)
γ(°)	80.7202 (13)
V(Å^3)	2535.84 (14)
Z	2
ρ(calc) [g cm^{-3}]	1.488
μ(Mo-Kα) (mm^{-1})	1.319
F(000)	1184
Crystal size (mm)	0.06 × 0.23 × 0.23
Temperature (K)	200
Radiation (Å)	0.71073
θ range (°)	1.4, 28.3
h, *k*, l	−13 : 13, −20 : 20, −23 : 23
Total reflections	123 842
Unique reflections	12 534 (R_{int} = 0.060)
Observed data [I > 2.0 σ(I)]	9294
*N*ref, *N*par	12 534, 600
R, wR_2, S	0.0370, 0.1119, 1.15
Largest diff. Peak, hole (e Å^3)	−0.61, 0.62

and structure refinement details are presented in Table 1. The molecular structure without hydrogen for clarity and short contact stacking is shown in Fig. S7. Selected bond lengths and bond angles of experimental and theoretical values are presented in Tables S1 and S2. The complex crystallized out in a *P*1 space group, a triclinic crystal system, suggesting that there was only one lattice point per unit cell. The structure formed a centrosymmetric dimeric unit of the zinc(II) dithiocarbamate complex. Each of the zinc(II) ions was coordinated to two 1-(4-methyl phenyl) piperazinyl-dithiocarbamate ligands in a bidentate chelating mode with one of the ligands concurrently bridging the other Zn(II) unit to form a five-coordinate geometry around each Zn(II) ion. The geometry around each zinc(II) ion is best described as a distorted square pyramidal geometry. The bond angles on the plane formed by the four sulfur atoms of both units were S11–Zn1–S21, 107.99(3)° and S32–Zn2–S41, 103.80(3)°. There was a weak adjacent Zn⋯S bridging interaction across the inversion center with slightly unequal Zn1⋯S42 and Zn2⋯S22 bond lengths at 2.394 Å and 2.396 Å, respectively.

This trend is similar to those of some reported dinuclear zinc(II) dithiocarbamate complexes, namely *N*,*N*-diallyldithiocarbamato-Zn(II),[42] *N*-ethyl-*N*-phenyl-dithiocarbamato-Zn(II),[43] and diallydithiocarbamato-Zn(II).[44] The Zn–S bond lengths are in the range of 2.36 Å–2.774 Å. The thioureide C–S and N–C bond lengths are in the range of 1.712 Å–1.754 Å and 1.314 Å–1.327 Å, respectively, similar to those observed in other dinuclear zinc(II) dithiocarbamate complexes.[42,45–47]

3.3. Structural optimization

The computationally refined and experimental geometries of the complex were compared (Fig. 3). Detailed comparisons of selected experimental bond lengths and angles with the calculated values are listed in Tables S1 and S2. The computationally optimized structure closely aligns with the experimentally determined single-crystal X-ray structure. The comparative experimental and theoretical values of the bond lengths and bond angles show minimal deviations. The mean absolute error (MAE) for the bond lengths is 0.042707 Å, and the mean square absolute error (MSAE) is 0.003557 Å, indicating that, on average, the calculated bond lengths are within 0.042707 Å of the experimental values. Similarly, the MAE for the bond angles is

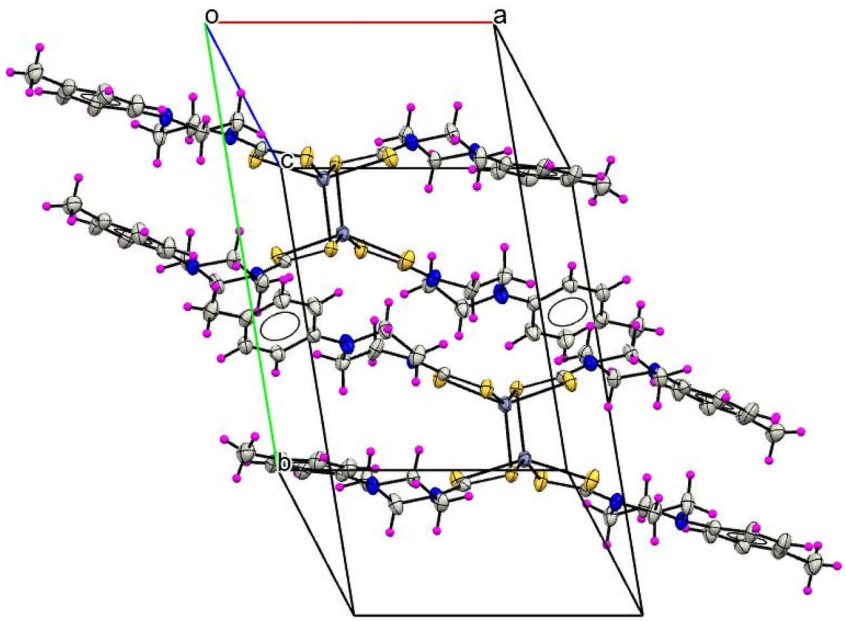

Fig. 2 Crystal packing of the 1-(4-methylphenyl)piperazinyl-dithiocarbamato Zn(II) complex view down reciprocal cell axis C.

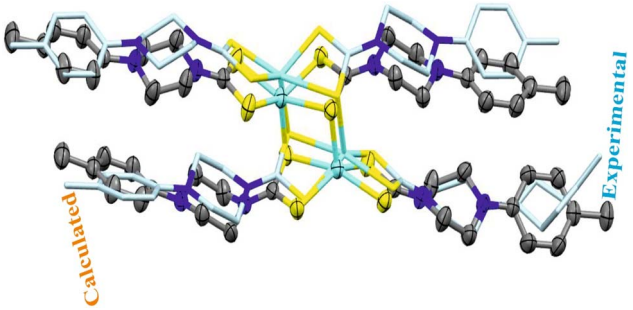

Fig. 3 Overlay of the experimental and optimized structures of 1-(4-methylphenyl)piperazinyl-dithiocarbamato Zn(II).

3.614103°, and the MSAE is 26.03925°, which indicates that, on average, the calculated bond angles are within 3.614103° of the experimental values. The negligible magnitude of errors between these values indicates a good fit for the computational model.[36,48] The comparative correlation between the experimental and calculated values is also demonstrated in the graphs shown in Fig. S8a and b for the bond lengths and angles, respectively. The graphs reveal R^2 coefficients of 0.9967 and 0.95438, respectively, indicating a strong agreement between the experimental and calculated structures.

3.4. Molecular interaction on Hirshfeld surface maps

The crystal structure was analysed using Crystal Explorer 17.5.[49,50] This analysis generates a surface based on the electron density associated with molecular contacts, specifically where the electron density of a molecule equals that contributed by a neighboring molecule.[51] Fig. 4 shows a 3D diagram of different interactions within the crystal lattice that highlights short contacts that are less than the sum of van der Waals radii. Fig. 4a displays the Hirshfeld surface mapped with a d_{norm} surface plot, showing atoms within a 3.80 Å radius cluster. The d_{norm} plot reveals diverse molecular surface properties. Red areas on the surface indicate strong piperazinyl-aryl (C–H···C), methyl–aryl (C–H···C), and aryl–sulfur (C–H···S) interactions. White areas indicate relatively weak interactions, including piperazinyl-aryl (C–H···H) and aryl–aryl (C–H···H) interactions. The blue regions indicate longer intermolecular contacts, while the white areas correspond to the approximation of the van der Waals radii. In addition, the red regions denote negative potential with electrophile characteristics, and the blue regions represent positive potential with nucleophile characteristics. Similarly, Fig. 4b depicts the Hirshfeld surface mapped with the shape index, where the red concave areas represent π···π cyclic stacking interactions, and the blue areas indicate ring atoms within the molecule. Fig. 4c shows the Hirshfeld surface mapped with curvedness, with flat regions indicating cyclic stacking interactions within the molecule.[51] Fig. 5 shows the 2D fingerprint plots of close contacts from the elements and surface maps. The plot suggests that crystal packing is dominated by H···H contacts, accounting for 54.7% of the interactions. Contributions from other contacts, including sulfur–hydrogen (S···H), carbon–oxygen (C···O), nitrogen–hydrogen (N···H), zinc–hydrogen (Zn…H), carbon–nitrogen (C···N), carbon–carbon (C···C), and carbon–sulfur (C···S), are 14.3%, 8.2%, 0.8%, 0.6%, 0.1%, and 0.3%, respectively. The graph of these contacts is shown in Fig. S6.

3.5. Electronic activities within the molecular orbitals

Frontier molecular orbital (FMO) analysis was used to examine the electronic activities within the highest occupied molecular orbital (HOMO) and the lowest unoccupied molecular orbital (LUMO) of a molecule. This reveals various molecular properties, including stability, chemical reactivity, and optical and electrical characteristics. The energy difference between these energy levels (HOMO–LUMO) or molecular orbitals is a key factor for understanding these properties and the chemical compound's general chemical behaviour.[52] Thus, a smaller energy gap signifies a more unstable and highly reactive molecule, which necessitates less excitation energy. In contrast, a bigger energy difference signifies stability and low reactivity.[53] In this study, the complex was identified as electron-rich, indicating an electron-donating capacity in the HOMO and an electron-accepting capacity in the LUMO, highlighting its potential in electron transfer chemical processes. Fig. 6 displays

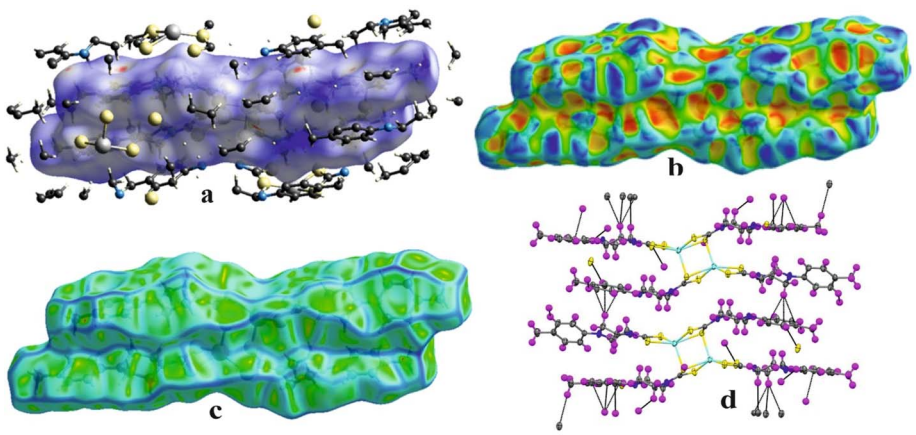

Fig. 4 Molecular interaction on the Hirshfeld surface mapped with d_{norm} and atoms within 3.80 radii contact (a), shape index (b), curvedness (c) and the crystal structure showing short contact < sum of vdW radii (d).

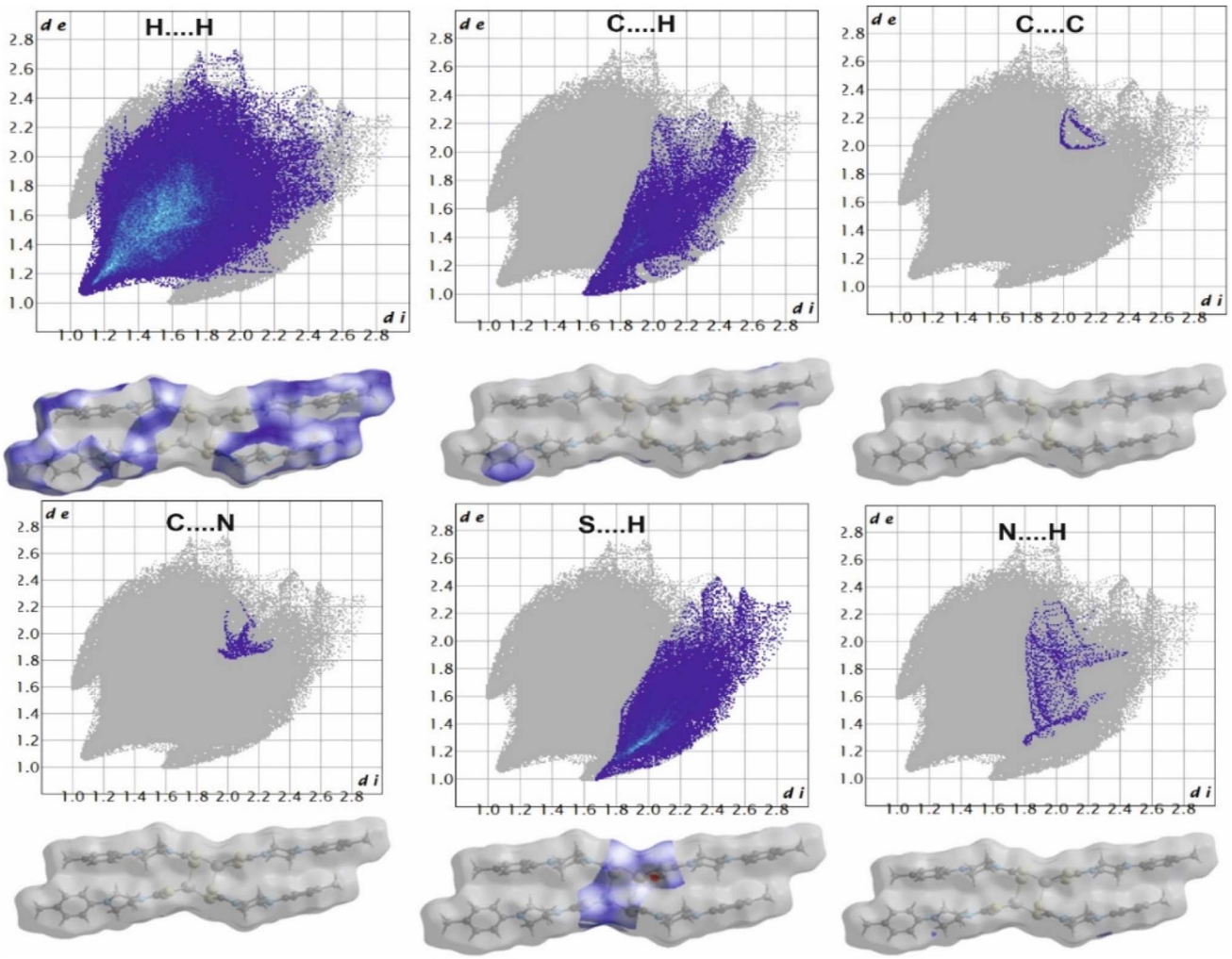

Fig. 5 2D fingerprint plots of the close contacts from elements and surfaces mapped with d_{norm}.

the HOMO–LUMO diagram of the complex, with green and red colors indicating the molecular orbitals (MOs); the green and red colors denote the negative and positive phases of the complex, respectively. The HOMO orbital is predominantly localized around the phenylpiperazine ring, suggesting that the π-electrons are spread around the molecule. Conversely, the LUMO orbital is primarily localized around the metal and thioureide. Thus, the energy gap (ΔE_{gap}) for this complex was determined from eqn (4) to be $\Delta E_{gap} = 3.7030$ eV, which indicates a reactive molecule. The detailed FMO reactivity parameters are presented in Table S3.

$$\Delta E_{gap} = E_{LUMO} - E_{HOMO} \quad (4)$$

3.6. Molecular electrostatic potential (MEP) and Mulliken charge distribution analysis

An MEP analysis was conducted to determine the distribution of electrons within the complex and how this distribution affects its electrostatic potential. The electron density map reveals where electrons are most located within the molecule, indicating regions of high and low electron density and their impact on the electrostatic potential around the molecule. This information provides insights into the compound's reactivity.[54,55] Regions of high electron density correspond to areas of negative electrostatic potential, which may attract positively charged species, while regions of low electron density might attract negatively charged species. Combining electron density with ESP mapping provides a comprehensive picture of a molecule's electronic environment, which is essential to understanding its chemical properties and reactions with other biomolecules.[56] In Fig. 7a, the region mapped in color indicates an electron-deficient area, making it favorable for nucleophilic attack. Conversely, the region mapped in red denotes an electron-rich area with a high concentration of electrons, making it susceptible to electrophilic attack.

Fig. 7b shows the Mulliken charge distribution indicating the partial charges on individual atoms. The charge was calculated using the electron on each atom. The positive atoms in green are electron-deficient, suggesting a loss of electron density relative to their neutral state, making them potential reactive sites, especially in nucleophilic reactions. These atoms

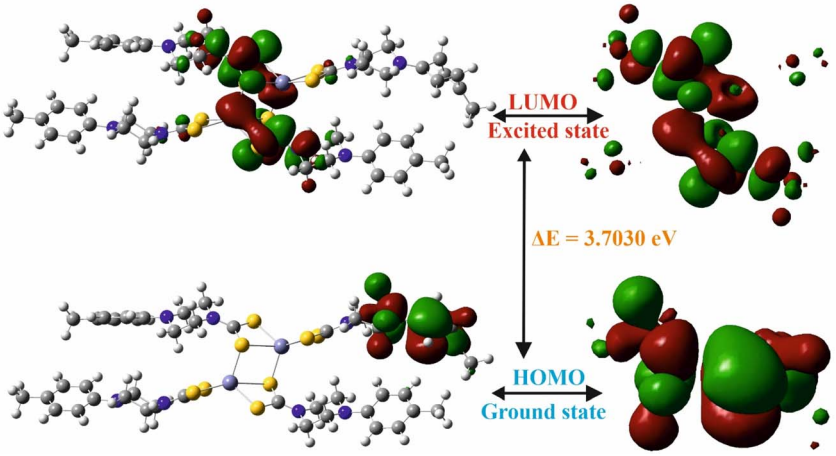

Fig. 6 HOMO–LUMO plots of the 1-(4-methylphenyl)piperazinyl-dithiocarbamato Zn(II) complex.

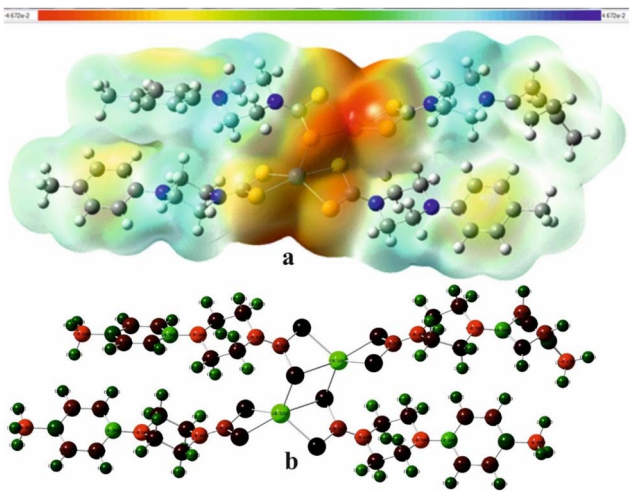

Fig. 7 Electron density from the total SCF density mapped with the ESP of the complex with the blue and red colours indicating the most positive and negative regions, respectively (a) and the Mulliken charge distribution (b).

contribute to areas of positive electrostatic potential around the molecule, which affect its interactions with charged species and its solvation behavior. Conversely, atoms with negative charges are bonded to less electronegative atoms, which reflect unequal electron sharing that makes them potential reactive sites, particularly in electrophilic reactions.[57,58] The hydrogen, nitrogen, and zinc atoms exhibit positive Mulliken charges, while the carbon atoms have negative charges. The increased electron density in the carbon atoms is due to the delocalization of π-electrons in the aryl and piperazinyl rings, resulting in negative Mulliken charges.

3.7. Powder X-ray diffraction (P-XRD) patterns of the zinc sulfide nanoparticles

In the P-XRD patterns of the as-synthesized ZnS nanoparticles (Fig. 8), the observed diffraction peaks for ZnS-HDA at 22.96°, 25.89°, 27.61°, 33.32°, 43.14°, 46.94°, 51.68°, 55.74° and 66.87° correspond to the (100), (002), (101), (200), (102), (110), (103), (112) and (202) planes of wurtzite ZnS, respectively. Similarly, ZnS-DDA exhibits peaks at 22.88°, 24.80°, 27.58°, 33.64°, 41.52°, and 48.69°, which correspond to (100), (002), (101), (200), (102) and (110) planes of wurtzite ZnS, respectively. ZnS-ODA shows peaks at 22.44°, 25.12°, 27.54°, 33.57°, 43.05°, 47.97°, 56.35°, and 66.60°, corresponding to (100), (002), (101), (200), (102), (110), (112), and (202) planes, respectively.

The X-ray diffraction analysis of the ZnS nanoparticles synthesized using different capping agents confirms that all the samples predominantly crystallize in the hexagonal crystalline wurtzite phase (JCPDS No. 36-1450).[59,60] The peaks marked with stars (☆) are indexed to the cubic zinc blende (sphalerite) crystalline phase of ZnS (JCPDS No. 05-0566),[61] which indicates the coexistence of a minor zinc blende phase, while the asterisks (*) indicate diffraction peaks from the hexadecylamine capping agents. The use of different capping agents results in distinct interactions with the surface of the ZnS nanoparticles during synthesis, thereby influencing nucleation and crystal growth dynamics.[62,63] These varying interactions result in differences in crystallite size, lattice strain and defect density, which are reflected in subtle shifts or the appearance or

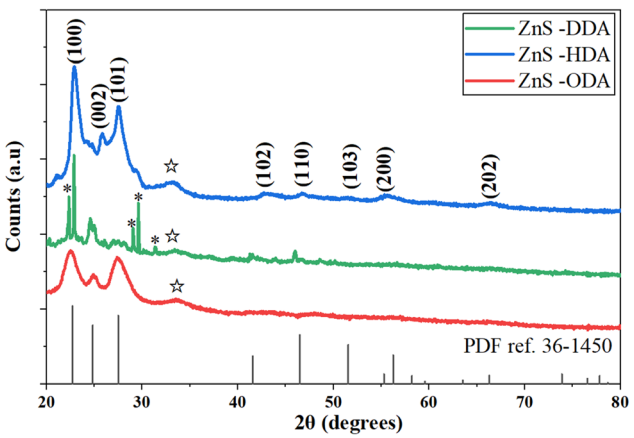

Fig. 8 P-XRD patterns of the ZnS nanoparticles.

disappearance of specific diffraction peaks. Notably, the diffraction patterns of ZnS-ODA and ZnS-HDA exhibit broad peaks, while ZnS-DDA shows narrow and sharp diffraction peaks, which may be due to the differences in crystallite size, strain, or disorder.[64]

The average crystallite size was calculated from the full width at half maximum (FWHM) of the (100) diffraction peak using the Debye–Scherrer equation. The FWHM and corresponding Bragg angle (θ) were obtained by fitting all the diffraction peaks with a Gaussian function. The calculated crystallite sizes for ZnS-DDA, ZnS-HDA, and ZnS-ODA were 2.79 nm, 4.84 nm, and 4.61 nm, respectively. Additionally, the lattice parameter, another crucial structural property derived from the diffractogram, was evaluated. Hexagonal wurtzite ZnS exhibits a standard lattice constant of 3.892 Å.[61] The calculated lattice constants for the as-prepared ZnS nanoparticles were 3.8787 Å, 3.8227 Å, and 3.9295 Å for ZnS-DDA, ZnS-HDA, and ZnS-ODA, respectively. These results indicate slight variations in the lattice parameters among the nanoparticles, as well as deviation from the standard ZnS value, which may be attributed to differences in crystallite size and the resulting lattice strain induced by the different capping agents.[65]

3.8. Morphological studies of the zinc sulfide nanoparticles

In the TEM micrographs of the zinc sulfide nanoparticles (Fig. 9), ZnS-DDA displays agglomerated quasi-spherical nanoparticles with an average particle size of 3.13 ± 0.83 nm and a narrow distribution. The short-chain DDA provides weak steric repulsion, resulting in high surface-energy nanocrystals that rapidly agglomerate because of van der Waals forces to minimize the exposed surface area.[66] However, the short ligand effectively suppresses Ostwald ripening, preserving small particle dimensions.[67] ZnS-HDA nanoparticles exhibit an agglomerated quasi-spherical and short rod-like morphology with an average particle size of 5.60 ± 2.10 nm. HDA provides partial steric stabilization, enabling preferential growth along the crystallographic axes, which gives rise to the mixed morphologies.[68] In contrast, ZnS-ODA nanoparticles are larger, irregularly shaped, and well-dispersed, with an average particle size of 10.44 ± 2.98 nm. The longest chain, ODA, forms a thick organic shell that provides steric hindrance.[69] This passivation prevents interparticle contact, promoting extended growth *via* Ostwald ripening and yielding highly dispersed nanoparticles.

The cross-sectional SEM micrographs and multi-element EDS mappings of the zinc sulfide nanoparticles (Fig. S10–12) revealed well-defined multi-layered rod-like particles with smooth surfaces (Fig. S10). ZnS-DDA has rock-like surface morphologies with hollow spheres, while ZnS-ODA has cloud-like surface morphologies with hollow spheres (Fig. S11 and 12). The EDS elemental mapping of the nanoparticles shows the composition of Zn, S and C. The percentages of Zn and S were found to be 48.38 and 51.62 for ZnS-HDA, 34.80 and 65.20 for ZnS-DDA and 11.33 and 25.98 for ZnS-ODA, respectively, as well as 62.69% of C in the case of ZnS-ODA. The high carbon content in ZnS-ODA is due to both the capping agent and carbon tape

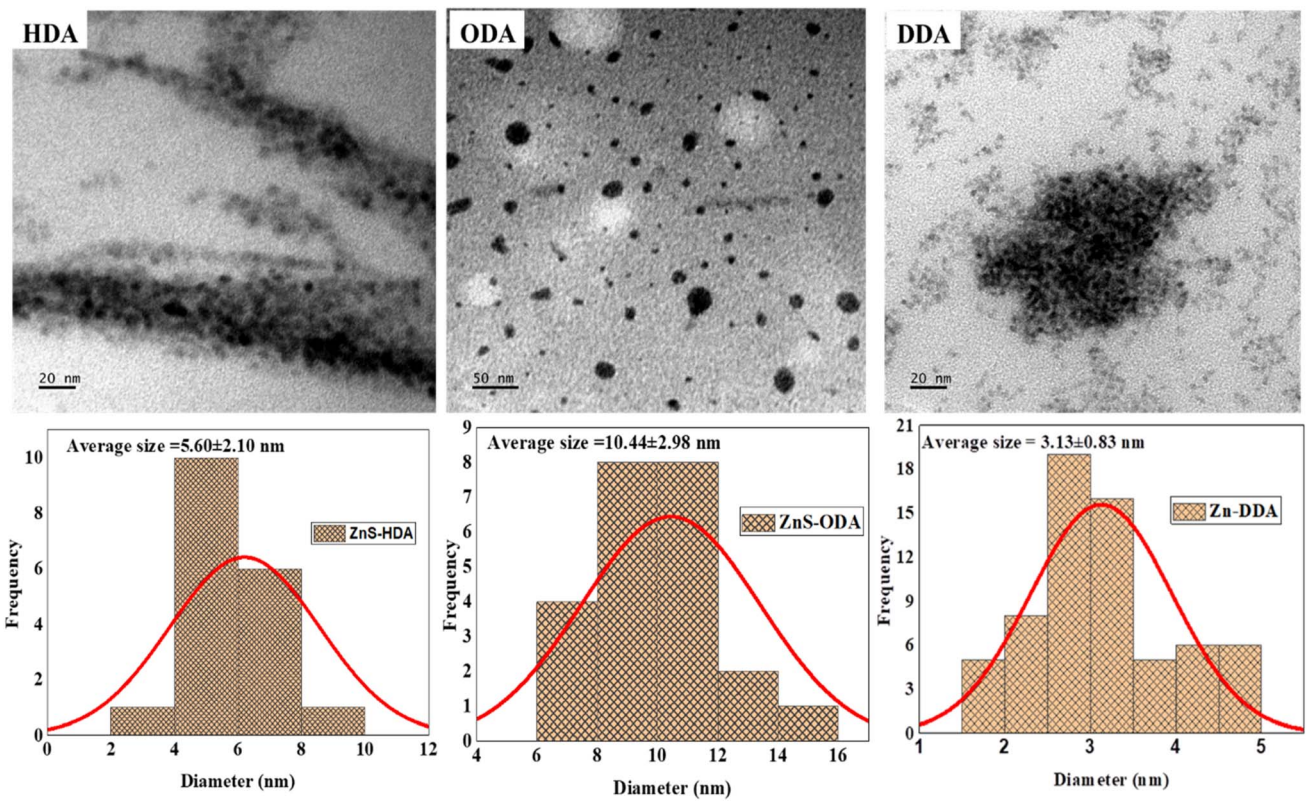

Fig. 9 TEM micrographs and particle size distribution histogram of the ZnS nanoparticles.

that was used for the sample preparation. The EDS mapping indicated that the Zn and S elements are ubiquitously distributed over the entire image, with blue and yellow coloration, respectively, in the case of the ZnS-HDA and ZnS-DDA nanoparticles. That of ZnS-ODA shows Zn, S, and C in turquoise blue, blue and yellow coloration, respectively. These results confirm the successful preparation of the ZnS nanoparticles.[70]

3.9. Optical absorption studies of the ZnS nanoparticles

The optical absorption spectra and energy band gap of the ZnS nanoparticles (Fig. S13–S15) revealed absorption band edges at 285 nm, 327 nm, and 285 nm for ZnS-ODA, ZnS-DDA, and ZnS-HDA, respectively. The absorption band edges are due to the excitation of electrons from the sulfur 3p orbitals in the valence band to the zinc 4s orbitals in the conduction band.[71] The energy bandgap of the nanoparticles was calculated using the Tauc plots. ZnS-HDA and ZnS-DDA exhibit band gap energies of 3.70 eV and 3.64 eV, respectively, which are lower than that of bulk wurtzite ZnS.[72] The reduction in band gaps is attributed to the surface defect states.[73,74] The defects, such as zinc and sulfur vacancies, in ZnS nanoparticles have been reported to enhance the generation of reactive oxygen species.[75] These vacancies create mid-gap states that serve as electron traps, thereby promoting the separation of electrons and holes.[76–78] In contrast, ZnS-ODA exhibited an energy bandgap of 3.93 eV, which is higher than that of bulk ZnS and can be attributed to quantum confinement effects.[79] The band gap energies of the as-prepared ZnS nanoparticles are comparable to those of other reported ZnS nanophotocatalysts.[80–82]

3.10. Photocatalytic degradation studies

The photocatalytic activities of the nanoparticles were evaluated by the degradation of 10 mg L^{-1} of trypan blue and rhodamine 6G dyes under visible light. The degradation spectra of the dyes are shown (Fig. S16 and S17). The degradation of the dyes with and without ZnS nanoparticles was evaluated. From the result, only 1.30% trypan blue dye and 1.39% rhodamine (Table 2) degradation was observed in the absence of the ZnS photocatalyst after 180 min. However, in the presence of the nanophotocatalyst, the percentage degradation of the dyes increased with time. Fig. 10 shows the percentage photocatalytic degradation of the dyes with time. It shows that ZnS-ODA, ZnS-DDA, and ZnS-HDA degraded 95.71%, 61.06%, and 73.19% of trypan blue dye, respectively (Fig. 10a). This suggests that the longer alkyl chain-capped ZnS nanoparticles enhance photocatalytic performance compared to DDA and HDA, which may be due to particle dispersion, reduced aggregation, and enhanced interfacial charge transfer.[83] The dispersion of ZnS-ODA ensures the maximum exposure of active surface sites and facilitates the efficient diffusion of dye molecules toward the catalyst,

Table 2 Percentage photodegradation, rate constant, and half-life of the as-prepared ZnS nanoparticles

Dye	Photocatalyst	% Photodegradation	Rate constant, k (min^{-1})	R^2 value	Half-life (min)
Trypan blue	Control	1.30	$6.95 \times 10^{-5} \pm 1.31 \times 10^{-5}$	0.8693	9.97×10^{3}
	ZnS-ODA	95.71	0.01688 ± 0.00112	0.9787	41.06
	ZnS-DDA	61.06	$0.00518 \pm 2.33 \times 10^{-4}$	0.9880	133.81
	ZnS-HDA	73.19	$0.00675 \pm 6.91 \times 10^{-4}$	0.9503	102.69
Rhodamine 6G	Control	1.39	$7.27 \times 10^{-5} \pm 1.20 \times 10^{-5}$	0.9857	9.53×10^{3}
	ZnS-ODA	47.83	0.00354 ± 0.00057	0.8854	195.80
	ZnS-DDA	83.21	0.00744 ± 0.00119	0.8874	93.16
	ZnS-HDA	71.53	0.00621 ± 0.00126	0.8501	111.61

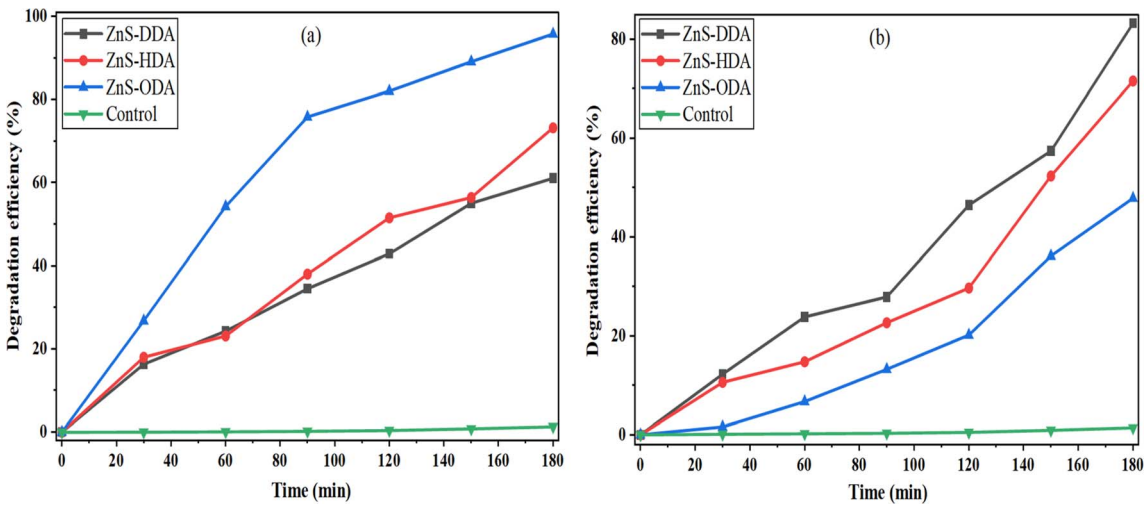

Fig. 10 Degradation efficiency curves of (a) trypan blue and (b) rhodamine 6G dyes.

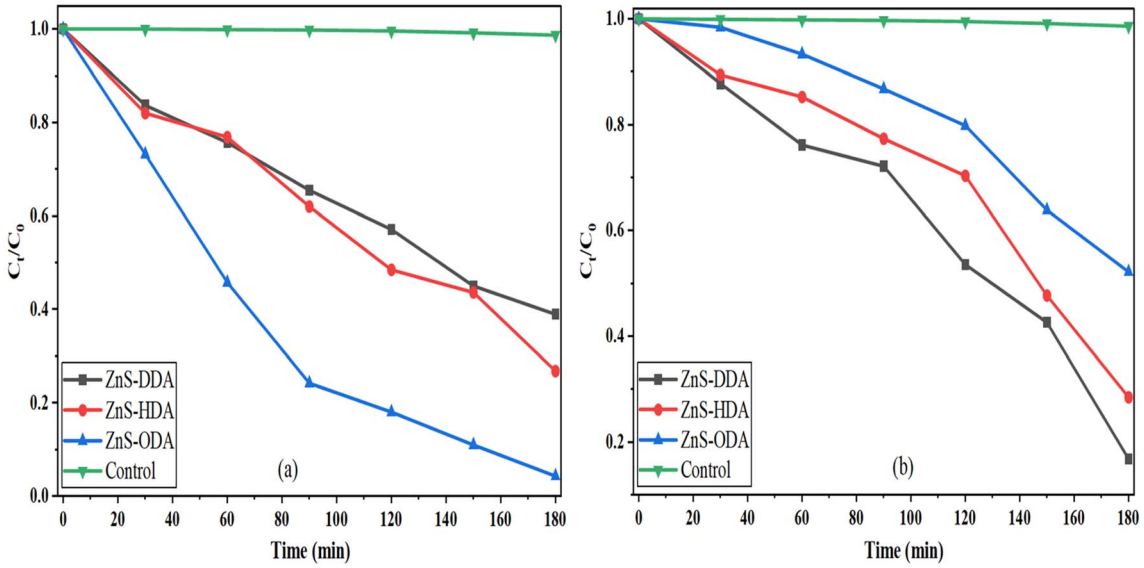

Fig. 11 Degradation of (a) trypan blue and (b) rhodamine 6G (C_t/C_0) with time.

contributing significantly to its superior photocatalytic performance against trypan blue.[84] Thus, 47.83%, 83.21%, and 71.53% of rhodamine 6G dye was degraded in the presence of ZnS-ODA, ZnS-DDA, and ZnS-HDA (Fig. 10b), respectively. ZnS-DDA demonstrated superior performance, indicating that the shorter alkyl chain-capped ZnS nanoparticles are more favourable for degrading cationic xanthene dye, which could be ascribed to their electrostatic attraction and adsorption affinity for the dye molecules.[85,86] Fig. 11 illustrates the progressive decrease in the changes in dye concentration, indicating their degradation with time.

The rate constant (k) observed for the trypan blue dye degradation from the linear fitted curves of natural logarithm of (C_0/C_t) *versus* time (Fig. 12) are 0.01688 min^{-1} (R^2 = 0.9787), 0.00518 min^{-1} (R^2 = 0.9880), and 0.00675 min^{-1} (R^2 = 0.9503) in the presence of ZnS-ODA, ZnS-DDA and ZnS-HDA, respectively. Similarly, rate constants (k) of 0.00354 min^{-1} (R^2 = 0.8854), 0.00744 min^{-1} (R^2 = 0.8874), and 0.00621 min^{-1} (R^2 = 0.8301) were observed for the Rhodamine dye degradation by ZnS-ODA, ZnS-DDA, and ZnS-HDA, respectively. ZnS-ODA exhibited the highest rate constant for trypan blue, while ZnS-DDA achieved the fastest degradation for rhodamine 6G. This is consistent with the degradation efficiency percentages. The high R^2 values (>0.85) confirm good adherence to first-order kinetics. The half-lives of the nanoparticles are high under controlled conditions, suggesting relatively slow degradation under photolysis.[87]

A comparison of the photocatalytic degradation of the dyes to that of reported nanoparticles is presented in Table 3. The ZnS nanophotocatalyst reported in the present study exhibits relatively good photocatalytic degradation efficiency and can,

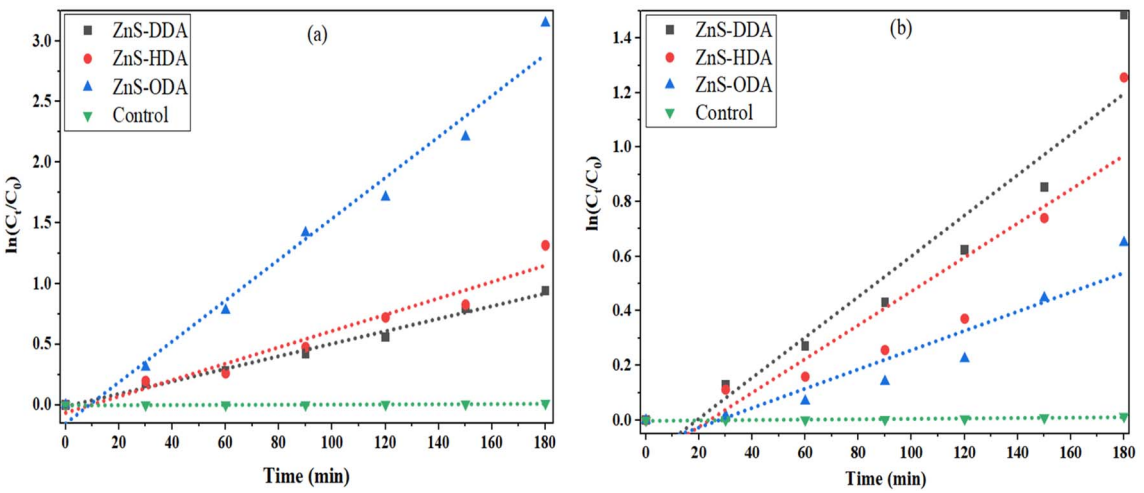

Fig. 12 Kinetic plots of (a) trypan blue and (b) rhodamine 6G.

Table 3 Comparison of percentage photodegradation of the dyes by the as-prepared ZnS nanoparticles and other metal sulfide-containing and allied nanoparticles

Photocatalyst	Irradiation time	Light source	% Degradation	Reference
Trypan blue dye				
$Bi_{2-x}Cu_xO_3$ NPs	48 min	W-lamp light	85.5%	88
Mercaptoacetic acid-capped SnS nanorods	4 h	Sunlight	95%	89
Ag_3PO_4/Bi_2S_3-HKUST-1-MOF	25 min	LED	98.44%	90
CuO	300 min	UV light	82.9%	28
PAN/α-FeOOH NFs	120 min	Solar light	99.7%	91
ZnO	120 min	Visible light	70%	92
ZnO:Ag nanoparticles	180 min		80%	92
ZnS-NPs	180 min	Visible light	96.39%	Present study
Rhodamine 6G dye				
Pc-$MnFe_2O_4$–TiO_2 fibers	270 min	Modulight® Medical Laser system	64.5%	93
3-g-C_3N_4–ZnO fibers	270 min	Modulight® Medical Laser system	96.7%	94
PANI/ZnS	60 min	UV light	80.62	95
Ni–Mn–S/rGO	150 min	Sunlight	93.2%	96
Ag–ZnS-MWCNTs	116 min	Visible light	87.53%	97
$(SnS)_3/(CdS)_1$-montmorillonite	360 min	Visible light	97%	98
ZnS-NPs	180 min	Visible light	84.22%	Present study

therefore, be used for the photodegradation of trypan blue and rhodamine 6G.

3.11. Influence of different reactive species on trypan blue and rhodamine 6G photocatalytic degradation

The influence of reactive species on the photocatalytic degradation of (a) trypan blue and (b) rhodamine 6G was evaluated using isopropyl alcohol (IPA) as a hydroxyl radical (˙OH) scavenger, silver nitrate (SN) as an electron (e^-) scavenger, and benzoquinone (BQ) as a superoxide radical ($˙O_2^-$) scavenger. The results are presented in Fig. S19(a) and (b). In the absence of scavengers, ZnS exhibited high degradation efficiency for both dyes. However, the degradation efficiency significantly decreased upon the addition of scavengers, suggesting that multiple reactive species contribute to the photocatalytic process. Upon introducing SN, a drastic decrease in the degradation efficiency was observed (11.24–21.67% for trypan blue and 3.59–17.02% for Rhodamine 6G), indicating that photogenerated electrons (e^-) play a major role in the photocatalytic reaction by facilitating the formation of $˙O_2^-$ *via* O_2 reduction.[99,100] The presence of BQ also suppressed the degradation efficiency to 3.83–13.02% for trypan blue and 7.04–18.34% for rhodamine 6G, indicating that $˙O_2^-$ radicals are major oxidative species for rhodamine 6G and secondary species for trypan blue. The addition of IPA also reduced the degradation efficiency to 4.63–9.91% for trypan blue and 2.08–9.67% for rhodamine 6G, suggesting that hydroxyl radicals (˙OH) are the primary reactive species in the degradation reaction for both dyes.[101] These results show that the photocatalytic degradation of trypan blue and rhodamine 6G by ZnS nanoparticles proceeds through oxidation and reduction reactions involving e^-, $˙O_2^-$, and ˙OH species generated upon light irradiation.

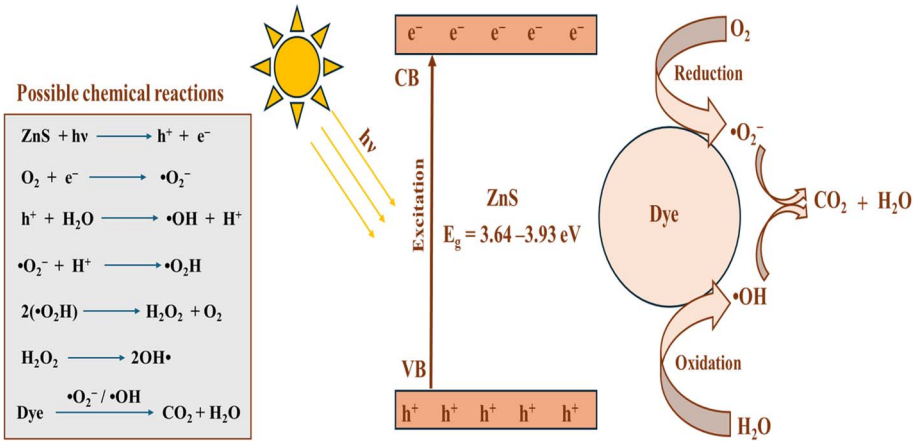

Scheme 1 Possible mechanism for the photocatalytic degradation of the trypan blue and rhodamine 6G dyes by ZnS-HDA, ZnS-DDA, and ZnS-ODA nanoparticles.

Scheme 1 illustrates the plausible mechanism for the photocatalytic degradation of the trypan blue and rhodamine 6G dyes. Upon irradiation by visible light with an energy equal to or greater than the bandgap of the ZnS nanoparticles, electrons in the valence band are promoted to the conduction band. This excitation generates electron–hole pairs on the catalyst surface, initiating redox reactions.[102] The excited electrons reduce the dissolved oxygen molecules to form superoxide radicals ($^{\bullet}O_2^-$), while the holes oxidize the water molecules to generate hydroxyl radicals ($^{\bullet}OH$). These reactive oxygen species undergo a series of reactions, ultimately breaking down the dye molecules into smaller, less harmful compounds like CO_2, water, and mineral salts.[103]

4. Conclusions

A 1-(4-methylphenyl)piperazinyl dithiocarbamato-*S*,*S*′ zinc(II) complex was prepared and characterized by single-crystal X-ray crystallography. The molecular structure reveals that the compound is a dimeric zinc(II) dithiocarbamate complex, where each zinc(II) ion coordinates to two molecules of the 1-(4-methyl phenyl)piperazinyl dithiocarbamato ligand in a bidentate chelating mode and is further bridged by the adjacent sulfur ion of the centrosymmetric ligand molecule. Computational molecular modelling of the optimized structure of the zinc(II) compound was performed to determine the correlation between the experimental and theoretical molecular and electronic properties. The theoretical results showed reasonable agreement with the experimental data. The complex was used as a single-source precursor and thermolyzed in octadecylamine (ODA), dodecylamine (DDA), and hexadecylamine (HDA) to prepare zinc sulfide nanoparticles: ZnS-ODA, ZnS-DDA, and ZnS-HDA. The ZnS nanoparticles were used as photocatalysts for the degradation of trypan blue and rhodamine 6G dyes, with 95.71% and 83.21% photocatalytic degradation efficiencies achieved after 180 minutes, respectively. The kinetic study confirmed a pseudo-first-order photodegradation model for the as-synthesized ZnS nanoparticles.

Conflicts of interest

We have no conflict of interest.

Data availability

The authors confirm that the data supporting the findings of this study are available within the article and its supplementary information (SI). Supplementary information: ^{1}H-NMR spectra of the 1-(4-methylphenyl)piperazinyl dithiocarbamate (Fig. S1); ^{13}C NMR spectra of the 1-(4-methylphenyl)piperazinyl dithiocarbamate (Fig. S2); ^{1}H 1-(4-methylphenyl)piperazinyl dithiocarbamate-*S*,*S*′ Zn(II) complex (Fig. S3); heteronuclear single quantum correlation (HSQC) NMR spectra (Fig. S4); 1-(4-methylphenyl)piperazinyl dithiocarbamate-*S*,*S*′ Zn(II) complex (Fig. S5); mass spectrum of 1-(4-methylphenyl)piperazinyl dithiocarbamate-*S*,*S*′ Zn(II) complex (Fig. S5); FTIR spectra of the ligand and the complex (A), UV-Vis spectra of the ligand and the complex (B1 and B2) (Fig. S6); short contact stacking viewed down crystallographic *a* axis (Fig. S7); contacts in 1-(4-methylphenyl)piperazinyl-dithiocarbamator Zn(II) complex (Fig. S8); correlation graphs between the optimized and experimental bond lengths (a) and bond angles (b) (Fig. S9); EM micrograph and multi-element EDS mapping of ZnS-HDA (Fig. S10); SEM micrograph and multi-element EDS mapping of ZnS-DDA (Fig. S11); SEM micrograph and multi-element EDS mapping of ZnS-ODA (Fig. S12); UV-visible spectrum and Tauc plot band gap for ZnS-DDA (Fig. S13); UV-visible spectrum and Tauc plot band gap for ZnS-HDA (Fig. S14); UV-visible spectrum and Tauc plot band gap for ZnS-ODA (Fig. S15); absorption spectra of rhodamine 6G degradation by ZnS nanoparticles (Fig. S16); absorption spectra of trypan blue degradation by ZnS (Fig. S17); effect of scavengers on the photocatalytic degradation of trypan blue (a) and rhodamine 6G (b) using ZnS-DDA, ZnS-HDA, and ZnS-ODA nanoparticles (Fig. S18); comparison of some selected SC-X-ray experimental and DFT calculated bond lengths (Table S1); comparison of some selected experimental and DFT calculated bond angles of the zinc(II) complex (Table S2); frontier molecular orbital reactivity parameters obtained from DFT (Table S3). See DOI: https://doi.org/10.1039/d5ra04748.

CCDC 2361759 contains the supplementary crystallographic data for this paper.[104]

Acknowledgements

This research was funded by the National Research Foundation (NRF) South Africa through the award of competitive support for rated researcher (Grant Number: CPRR23042396404).

References

1 C. L. Yadav, M. G. B. Drew, K. Kumar and N. Singh, *Inorg. Chem.*, 2021, **60**, 6446–6462.
2 L. Kubens, K.-N. Truong, C. W. Lehmann, D. Lützenkirchen-Hecht, J. Bornhorst and F. Mohr, *Chem.–Eur.J.*, 2023, **29**, e202301721.
3 V. K. Maurya, L. B. Prasad, A. Singh, K. Shiv and A. Prasad, *J. Sulphur Chem.*, 2023, **44**, 336–353.
4 J. M. Veiga-del-Baño, S. Martínez-López, G. Pérez-Lucas, J. J. Cuenca-Martínez and P. Andreo-Martínez, *Chemosphere*, 2023, **313**, 137342.
5 A. Singh, K. Shiv, R. Singh, M. K. Bharty, P. P. Manna and L. B. Prasad, *Dalton Trans.*, 2024, **53**, 1196–1208.
6 M. M. Gul, K. S. Ahmad, A. G. Thomas and M. K. Okla, *Ionics*, 2024, **30**, 1587–1602.
7 J. C. Sarker and G. Hogarth, *Chem. Rev.*, 2021, **121**, 6057–6123.
8 J. C. Sarker, X. Xu, F. Alam, R. Nash, S. Boonrungsiman, D. Pugh, J. K. Cockcroft, D. J. Lewis and G. Hogarth, *New J. Chem.*, 2023, **47**, 12718–12727.
9 Q. Su, Y. Xie, M. Chen, X. Xue and X. Cui, *J. Colloid Interface Sci.*, 2022, **622**, 562–576.
10 H.-U. Islam, A. Roffey, N. Hollingsworth, W. Bras, G. Sankar, N. H. De Leeuw and G. Hogarth, *Nanoscale Adv.*, 2020, **2**, 798–807.

11 A. Khan, F. Hayat, I. S. Butler, M. Nawaz Tahir and Z. u. Rehman, *Polyhedron*, 2021, **193**, 114876.
12 J. C. Sarker, F. Alam, P. McNaughter, D. Pugh, J. K. Cockcroft, D. J. Lewis and G. Hogarth, *Inorg. Chim. Acta*, 2023, **556**, 121663.
13 H. S. Dar, I. A. Ansari, S. Tabrez, M. Rana, M. Usman, S. Ul Islam, A. Rub and Rahisuddin, *Polyhedron*, 2021, **208**, 115424.
14 E. Sathiyaraj and S. Thirumaran, *Chem. Phys. Lett.*, 2020, **739**, 136972.
15 P. Selvaganapathi, S. Thirumaran and S. Ciattini, *Polyhedron*, 2018, **149**, 54–65.
16 H. Kaur, S. Kumar, P. Kumar, A. A. Ghfar and G. Bouzid, *Environ. Res.*, 2024, **259**, 119534.
17 S. N. Shukla, P. Gaur and N. Rai, *Appl. Nanosci.*, 2015, **5**, 583–593.
18 H. S. I. Sullivan, J. D. Parish, P. Thongchai, G. Kociok-Köhn, M. S. Hill and A. L. Johnson, *Inorg. Chem.*, 2019, **58**, 2784–2797.
19 G. Kathiresan, K. Vijayakumar, A. P. Sundarrajan, H.-S. Kim and K. Adaikalam, *Optik*, 2021, **238**, 166671.
20 E. Sathiyaraj, M. V. Perumal, E. R. Nagarajan and C. Ramalingan, *J. Saudi Chem. Soc.*, 2018, **22**, 527–537.
21 Q. Zhu, Q. Xu, M. Du, X. Zeng, G. Zhong, B. Qiu and J. Zhang, *Adv. Mater.*, 2022, **34**, 2202929.
22 R. Sasikala, K. Karthikeyan, D. Easwaramoorthy, I. M. Bilal and S. K. Rani, *Environ. Nanotechnol., Monit. Manage.*, 2016, **6**, 45–53.
23 H. H. Sornaly, S. Ahmed, K. F. Titin, M. N. Islam, A. Parvin, M. A. Islam, H. M. Faruquee, K. K. Biswas, R. Islam, D. K. Paul and S. K. Biswas, *Sustainable Chem. Pharm.*, 2024, **39**, 101538.
24 A. Tkaczyk, K. Mitrowska and A. Posyniak, *Sci. Total Environ.*, 2020, **717**, 137222.
25 B. Haridevamuthu, R. Murugan, B. Seenivasan, R. Meenatchi, R. Pachaiappan, B. O. Almutairi, S. Arokiyaraj, K. M. Kathiravan and J. Arockiaraj, *J. Hazard. Mater.*, 2024, **461**, 132524.
26 H. B. Slama, A. Chenari Bouket, Z. Pourhassan, F. N. Alenezi, A. Silini, H. Cherif-Silini, T. Oszako, L. Luptakova, P. Golińska and L. Belbahri, *Appl. Sci.*, 2021, **11**, 6255.
27 T. A. Khattab, M. S. Abdelrahman and M. Rehan, *Environ. Sci. Pollut. Res.*, 2020, **27**, 3803–3818.
28 E. Brillas and R. Oliver, *Chemosphere*, 2024, **355**, 141766.
29 J. M. Chacón, M. Teresa Leal, M. Sánchez and E. R. Bandala, *Dyes Pigm.*, 2006, **69**, 144–150.
30 K. K. Chenab, B. Sohrabi, A. Jafari and S. Ramakrishna, *Mater. Today Chem.*, 2020, **16**, 100262.
31 N. Gupta, A. L. S. Chandel, M. Mehta and A. Tiwari, *Results Chem.*, 2024, **7**, 101242.
32 P. A. Ajibade, F. P. Andrew, T. B. Mbuyazi, T. R. Papo, F. I. Danladi, A. Rawat, C. Zhang and K. Rajeshwar, *ACS Omega*, 2025, **10**, 45090–45102.
33 O. Dolomanov, L. Bourhis, R. Gildea, J. Howard and H. Puschmann, *J. Appl. Crystallogr.*, 2009, **42**, 339–341.
34 G. Sheldrick, *Acta Crystallogr., Sect. A*, 2015, **71**, 3–8.
35 G. M. Sheldrick, *Acta Crystallogr., Sect. A*, 2015, **71**, 3–8.
36 A. H. Bakheit, H. A. Abuelizz and R. Al-Salahi, *Crystals*, 2023, **13**, 1410.
37 M. J. Frisch, G. W. Trucks, H. B. Schlegel, G. E. Scuseria, M. A. Robb, J. R. Cheeseman, G. Scalmani, V. Barone, G. A. Petersson, H. Nakatsuji, X. Li, M. Caricato, A. V. Marenich, J. Bloino, B. G. Janesko, R. Gomperts, B. Mennucci, H. P. Hratchian, J. V. Ortiz, A. F. Izmaylov, J. L. Sonnenberg, D. Williams-Young, F. Ding, F. Lipparini, F. Egidi, J. Goings, B. Peng, A. Petrone, T. Henderson, D. Ranasinghe, V. G. Zakrzewski, J. Gao, N. Rega, G. Zheng, W. Liang, M. Hada, M. Ehara, K. Toyota, R. Fukuda, J. Hasegawa, M. Ishida, T. Nakajima, Y. Honda, O. Kitao, H. Nakai, T. Vreven, K. Throssell, J. A. Montgomery Jr, J. E. Peralta, F. Ogliaro, M. J. Bearpark, J. J. Heyd, E. N. Brothers, K. N. Kudin, V. N. Staroverov, T. A. Keith, R. Kobayashi, J. Normand, K. Raghavachari, A. P. Rendell, J. C. Burant, S. S. Iyengar, J. Tomasi, M. Cossi, J. M. Millam, M. Klene, C. Adamo, R. Cammi, J. W. Ochterski, R. L. Martin, K. Morokuma, O. Farkas, J. B. Foresman and D. J. Fox, *Gaussian 16 Rev. C.01*, 2016.
38 D. E. Kiven, F. K. Bine, N. K. Nkungli, A. D. Tamafo Fouegue, S. N. Tasheh and J. N. Ghogomu, *RSC Adv.*, 2024, **14**, 18646–18662.
39 S. Eswari, P. Lakshmanan and S. Thirumaran, *J. Mol. Struct.*, 2023, **1276**, 134805.
40 A. Singh, R. Kumar, K. Shiv, S. K. Pandey, M. K. Bharty, R. J. Butcher and L. B. Prasad, *J. Mol. Struct.*, 2024, **1298**, 137052.
41 R. Irfandi, I. Raya, A. Ahmad, A. Fudholi, Riswandi, S. Santi, W. P. Azalea, S. E. Putri, M. N. Alam, U. Supratman, S. O. Olubode, E. A. Abdalrazaq, M. Kandeel, N. H. Soekamto, H. Natsir, Maming and Ramlawati, *Mol. Diversity*, 2024, **28**, 3199–3214.
42 S. Tetteh, *Cryst. Growth Des.*, 2024, **24**, 506–513.
43 P. A. Ajibade, J. Z. Mbese and B. Omondi, *Inorg. Nano-Met. Chem.*, 2017, **47**, 202–212.
44 P. A. Ajibade, T. B. Mbuyazi and A. M. Paca, *ACS Omega*, 2023, **8**, 24750–24760.
45 M. Shahid, T. Rüffer, H. Lang, S. A. Awan and S. Ahmad, *J. Coord. Chem.*, 2009, **62**, 440–445.
46 F. A. Almeida Paz, M. C. Neves, T. Trindade and J. Klinowski, *Acta Crystallogr., Sect. E:Crystallogr. Commun.*, 2003, **59**, m1067–m1069.
47 E. R. T. Tiekink, *Crystals*, 2018, **8**, 292.
48 R. Kerkour, O. Moumeni, N. El houda Rabhi, M. Mehri, A. Boublia, N. Chafai and S. Chafaa, *J. Mol. Struct.*, 2024, **1315**, 138842.
49 Y. Laamari, M. Fawzi, M. E. Hachim, A. Bimoussa, A. Oubella, E. M. Ketatni, M. Saadi, L. E. Ammari, M. Y. A. Itto, H. Morjani, M. Khouili and A. Auhmani, *J. Mol. Struct.*, 2024, **1297**, 136864.
50 J.-Y. Tong, L.-J. Min, N.-B. Sun, H.-K. Wu, S.-J. Yu and Q. Bian, *Chem. Biol. Technol. Agric.*, 2025, **12**, 134.
51 Y. O. Bhola, B. N. Socha, S. B. Pandya, R. P. Dubey and M. K. Patel, *Mol. Cryst. Liq. Cryst.*, 2019, **692**, 83–93.

52 S. Janani, H. Rajagopal, S. Muthu, S. Aayisha and M. Raja, *J. Mol. Struct.*, 2021, **1230**, 129657.
53 S. Gul, F. Jan, A. Alam, A. Shakoor, A. Khan, A. F. AlAsmari, F. Alasmari, M. Khan and L. Bo, *Sci. Rep.*, 2024, **14**, 3419.
54 C. H. Suresh, G. S. Remya and P. K. Anjalikrishna, *Wiley Interdiscip. Rev.:Comput. Mol. Sci.*, 2022, **12**, e1601.
55 A. R. Kumar, L. Ilavarasan, G. P. S. Mol, S. Selvaraj, M. Azam, P. Jayaprakash, M. Kesavan, M. Alam, J. Dhanalakshmi, S. I. Al-Resayes and A. Ravi, *J. Mol. Struct.*, 2024, **1298**, 136974.
56 R. Bhavani, S. Elangovan, G. Suresh, S. Sankar, N. Kanagathara and P. Revathi, *Inorg. Chem. Commun.*, 2024, **165**, 112584.
57 A. Saral, A. Manikandan, S. Javed and S. Muthu, *Chem. Phys. Impact.*, 2024, **8**, 100392.
58 H.-L. An, Y. Duan, T.-T. Chen and L.-Q. Chai, *J. Mol. Struct.*, 2024, **1310**, 138320.
59 Y. Piña-Pérez, E. Samaniego-Benítez, J. H. Sierra-Uribe, F. González, F. Tzompantzi, L. Lartundo-Rojas and Á. Mantilla, *J. Environ. Chem. Eng.*, 2023, **11**, 109760.
60 X. Zhang, D. Kim and L. Y. S. Lee, *ACS Appl. Energy Mater.*, 2021, **4**, 2586–2592.
61 R. Mendil, Z. Ayadi, J. Benbelgacem and K. Djessas, *J. Mater. Sci.:Mater. Electron.*, 2016, **27**, 444–451.
62 A. Chakrabarti and E. Alessandri, *Appl. Nanosci.*, 2024, **5**, 116–142.
63 Z. Montaseri, A. M. Tamaddon, M. J. Raee and F. A.-O. Farvadi, *ChemistryOpen*, 2023, **12**, e202300094.
64 P. Sagar, N. Sinha and B. Kumar, *J. Cryst. Growth*, 2024, **632**, 127646.
65 J. Díaz-Reyes, R. S. Castillo-Ojeda, R. Sánchez-Espíndola, M. Galván-Arellano and O. Zaca-Morán, *Curr. Appl. Phys.*, 2015, **15**, 103–109.
66 N. Petersen, M. Girard, A. Riedinger and O. Valsson, *Nano Lett.*, 2022, **22**, 9847–9853.
67 J. Choi and B. H. Kim, *Nanomaterials*, 2024, **14**, 1685.
68 M. Le Goas, J. Saber, S. G. Bolívar, J.-M. Rabanel, J.-M. Awogni, D. C. Boffito and X. Banquy, *Nano Today*, 2022, **45**, 101516.
69 L. Spitzmüller, J. Berson, T. Schimmel, T. Kohl and F. Nitschke, *Sci. Rep.*, 2024, **14**, 19222.
70 M. S. Elnouby, O. El-Shazly, E. F. El-Wahidy, M. Ramadan, A. A. M. Farag and N. Roushdy, *Optik*, 2023, **287**, 171070.
71 M. B. Asfia and M. Abdur Rashid, *Phys. B*, 2022, **646**, 414335.
72 L. Dai, R. Lesyuk, A. Karpulevich, A. Torche, G. Bester and C. Klinke, *J. Phys. Chem. Lett.*, 2019, **10**, 3828–3835.
73 N. Prasad and B. Karthikeyan, *Nanotechnology*, 2019, **30**, 485702.
74 M. Bhushan, R. Jha and R. Bhardwaj, *J. Phys. Chem. Solids*, 2019, **135**, 109021.
75 A. Tiwari, S. Bishnoi and S. J. Dhoble, *J. Mol. Struct.*, 2026, **1349**, 143750.
76 K. Mróz, M. Kobielusz, Ł. Orzeł and W. Macyk, *J. Phys. Chem. C*, 2023, **127**, 17366–17376.
77 E. M. Jubeer, M. A. Manthrammel, P. A. Subha, M. Shkir, K. P. Biju and S. A. AlFaify, *Sci. Rep.*, 2023, **13**, 16820.
78 X. Hao, Y. Wang, J. Zhou, Z. Cui, Y. Wang and Z. Zou, *Appl. Catal., B*, 2018, **221**, 302–311.
79 D. C. Deka, A. Kalita, S. Bardaloi and M. P. C. Kalita, *J. Lumin.*, 2019, **210**, 269–275.
80 R. A. Khaparde, S. A. Acharya, P. Tumram and S. Sayyed, *J. Mol. Struct.*, 2025, **1329**, 141452.
81 S. Ouni, N. Bel Haj Mohamed, M. Bouzidi, A. Bonilla-Petriciolet and M. Haouari, *J. Environ. Chem. Eng.*, 2021, **9**, 105915.
82 H. R. Rajabi and M. Farsi, *Mater. Sci. Semicond. Process.*, 2016, **48**, 14–22.
83 G. Xie, L. Wang, Q. Zhu, Z. Chu, S. Tian, Z. Gui, K. Song and Z. Yu, *ACS Appl. Mater. Interfaces*, 2022, **14**, 57428–57439.
84 B. Arkhurst, D. Gunawan, L. Oppong-Antwi, R. Guo, A. N. Ashong, X. Fan, G. Bahmanrokh and S. L. I. P. Chan, *Appl. Surf. Sci.*, 2025, **708**, 163664.
85 A. P. Yepseu, T. Girardet, L. D. Nyamen, S. Fleutot, K. I. Y. Ketchemen, F. Cleymand and P. T. Ndifon, *Catalysts*, 2022, **12**, 61.
86 X.-Z. Guo, S.-S. Han, J.-M. Yang, X.-m. Wang, S.-S. Chen and S. Quan, *Ind. Eng. Chem. Res.*, 2020, **59**, 2113–2122.
87 C. Dalal, A. K. Garg, N. Jain, A. R. Naziruddin, R. K. Prajapati, S. K. Choudhary and S. K. Sonkar, *Sol. Energy*, 2023, **251**, 315–324.
88 H. A. Alsalmah, *Inorg. Chem. Commun.*, 2024, **163**, 112270.
89 D. Das and R. K. Dutta, *J. Colloid Interface Sci.*, 2015, **457**, 339–344.
90 S. Mosleh, M. R. Rahimi, M. Ghaedi and K. Dashtian, *Ultrason. Sonochem.*, 2016, **32**, 387–397.
91 A. Sudapalli and N. Shimpi, *Langmuir*, 2023, **39**, 15517–15534.
92 T. N. Ravishankar, K. Manjunatha, T. Ramakrishnappa, G. Nagaraju, D. Kumar, S. Sarakar, B. S. Anandakumar, G. T. Chandrappa, V. Reddy and J. Dupont, *Mater. Sci. Semicond. Process.*, 2014, **26**, 7–17.
93 S. T. Mkhondwane, S. Mgidlana, Y. Openda, N. Nwahara and T. Nyokong, *Catal. Today*, 2024, **432**, 114644.
94 S. T. Mkhondwane, S. Mgidlana and T. Nyokong, *J. Photochem. Photobiol.*, 2024, **447**, 115245.
95 S. Allahveran and A. Mehrizad, *J. Mol.Liq.*, 2017, **225**, 339–346.
96 N. Kandhasamy, G. Murugadoss, T. Kannappan, K. Kirubaharan, R. K. Manavalan, S. Devanesan, M. S. AlSalhi, R. Mythili, S. Shinde and H. M. Yadav, *Carbon Lett.*, 2024, **34**, 827–840.
97 E. B. Yazdani and A. Mehrizad, *J. Mol. Liq.*, 2018, **255**, 102–112.
98 C. Suppaso, N. Pongkan, S. Intachai, Y. Inchongkol, S. Bureekaew and N. Khaorapapong, *Appl. Clay Sci.*, 2023, **241**, 106999.
99 E. Ghiasi and A. Malekzadeh, *J. Inorg. Organomet. Polym.*, 2020, **30**, 2789–2804.

100 Y. Cui, Y. Li, Y. Liu, D. Shang, Y. Liu, L. Xie, S. Zhan and W. Hu, *Chem. Commun.*, 2022, **58**, 4251–4254.
101 H. Abbasi_Asl, Z. Moradi, M. Ghaedi and M. M. Sabzehmeidani, *J. Photochem. Photobiol.*, 2020, **401**, 112755.
102 A. Iqbal, A. Yusaf, M. Usman, T. Hussain Bokhari and A. Mansha, *Int. J. Environ. Anal. Chem.*, 2024, **104**, 5503–5537.
103 M. Surana, D. S. Pattanayak, V. Yadav, V. K. Singh and D. Pal, *Environ. Res.*, 2024, **247**, 118268.
104 CCDC 2361759: Experimental Crystal Structure Determination, 2025, DOI: 10.5517/ccdc.csd.cc2k8ls7.